

Femtosecond phase-space correlations in few-particle photoelectron pulses

Rudolf Haindl,^{1,2} Valerio Di Giulio,^{1,2,*} Armin Feist,^{1,2} and Claus Ropers^{1,2,†}

¹Max Planck Institute for Multidisciplinary Sciences, D-37077 Göttingen, Germany

²4th Physical Institute - Solids and Nanostructures, University of Göttingen, D-37077 Göttingen, Germany

(Dated: December 17, 2024)

Coulomb interactions impose fundamental limits on the brightness of continuous and pulsed electron beams. When multiple electrons leave a field emitter within a space-time volume of femtoseconds and nanometers, their mutual repulsion creates well-defined correlations in energy and time. Such correlations remain undetected in ensemble measurements that average over the statistics of the emission process. Here, we employ event-based and femtosecond-gated detection of photoelectron states to map Coulomb-correlated few-particle phase-space distributions. Inelastic electron-light scattering experiments performed on two-electron states reveal a bimodal structure in longitudinal phase space. Reconstructing the phase-space density, we find an overall energy-time dispersion that is distinct from that of the two separated sub-ensembles forming the bimodal distribution. Our findings disentangle correlation-induced and dispersive contributions to the energy-time structure of few-electron pulses and promote future electron microscopy schemes enhanced by multi-electron states.

The Coulomb interaction among electrons forming a beam remains a longstanding challenge for electron microscopy and spectroscopy. Limiting contrast and resolution, longitudinal [1] and transverse [2] scattering manifests as anticorrelations in the time of arrival [3] as well as the transverse position and momentum [4–8] at the detector plane. In pulsed electron beams produced by photoemission from nanotip field-emitters [9–11], event-based detection recently uncovered pronounced Coulomb-induced energy correlations in an electron microscope [8] and at free-standing nanotips [12]. The understanding of such correlations promote novel measurement schemes based on controlled few-electron states, underlying recent proposals of shot noise-reduced imaging [8, 13] and multi-particle sample excitations [14–23]. Moreover, multi-electron states are expected to enhance dose-sensitive imaging [24, 25] and quantum-mechanical electron-light entanglement [26–30].

The phase-space distribution of pulsed electron beams is particularly relevant in the context of ultrafast electron microscopy combining high temporal and spatial resolutions [31–38]. On the one hand, typically low duty cycles in ultrafast imaging, diffraction and spectroscopy aim for maximum allowable pulse charge, which renders Coulomb interactions an essential constraint in this technology. On the other hand, ultrafast microscopes offer ideal conditions to study the correlations among few-electron ensembles within a well-defined temporal gate. Several effects govern the spectral and temporal distribution of electron pulses, which involve the photoemission process [9–11, 39–43] as well as Coulomb interactions [8, 33, 44–46]. Measurements of the time structure of electron pulses can be obtained by electron-laser cross-correlation using ponderomotive scattering [47] or streaking [48, 49], recently performed for few-electron states [37]. Femtosecond-resolved temporal slicing [32, 33, 50, 51] based on inelastic electron-light interaction [52–54] has shown a broadening of the phase-space distribution with increasing average current. However, mean-field and

stochastic interactions are expected to affect pulse dispersion in distinct ways, which calls for the measurement of electron-number specific phase-space distributions.

In this letter, we present the measurement of multimodal phase-space distributions of Coulomb-correlated few-electron pulses. Using femtosecond gating in an Ultrafast Transmission Electron Microscope (UTEM), we record time-energy correlation maps of two-electron pulses and reconstruct their phase-space distribution. To corroborate our experimental findings, we formulate inelastic electron-light scattering in the multi-electron regime and perform numerical simulations reproducing the observed correlations in energy and time-of-arrival

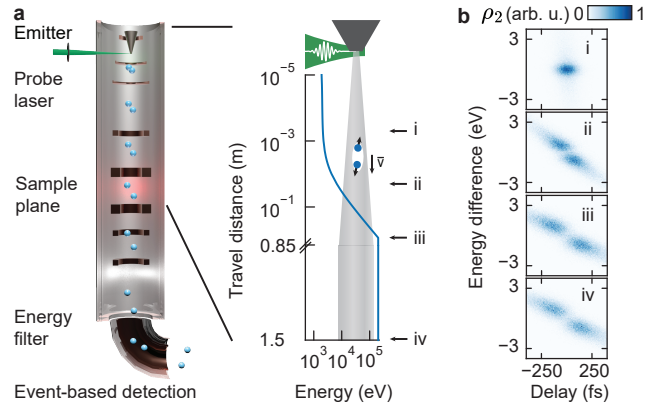


Figure 1. Generation and propagation of two-electron pulses in a field-emitter Ultrafast Transmission Electron Microscope (UTEM). (a) Schematic of the increasing temporal separation of a Coulomb-correlated photoelectron pair (left) accelerated to 200 keV energy (right) and recorded using an event-based detector behind an electron spectrometer. Note the logarithmic position scale during acceleration. (b) Simulated evolution of the longitudinal phase-space distribution for different locations along the microscope column (indicated by i-iv), illustrating the concurrent buildup of energy correlations and dispersive pulse broadening.

at the sample plane.

Optimized electron pulse properties are of central importance in ultrafast electron microscopy. In principle, the longitudinal properties of multi-electron ensembles are fully described by the $2N$ -dimensional phase-space density $\rho_N(\{t_i\}, \{E_i\})$, where $\{t_i\}$ and $\{E_i\}$ denote the set of N time and energy variables, respectively. Due to the high dimensionality of $\rho_N(\{t_i\}, \{E_i\})$, marginal phase-space densities are often sufficient in the analysis of beam properties and the determination of achievable energy and time resolution. These may be expressed in terms of the overall densities $\rho(t, E)$, or number-sorted as $\rho_N(t, E)$. In particular, the former results from the marginalization of $\rho_N(\{t_i\}, \{E_i\})$ with respect to the total number of electrons employed in the experiment, while the latter refers only to pulses containing N electrons.

This study aims at characterizing the number-sorted phase-space properties of few-electron pulses within a field-emitter UTEM (see Fig. 1a). In order to illustrate the Coulomb- and propagation-induced emergence of energetic and temporal correlations, we first show the results of two-electron trajectory simulations predicting the evolution of $\rho_2(t, E)$ along different positions in the microscope (see Appendix A). Upon photoemission, the initial conditions of the double-electron pulse in time and energy are normally distributed (Fig. 1b, panel i), that is, we assume no nascent correlations. Subsequently, the electrons are electrostatically accelerated along the beam direction. To a good approximation, the momentary rate of Coulomb-induced energy exchange is given by the Coulomb force times the mean velocity of the two electrons, which leads to an increasing difference in kinetic energy (panel ii). The external accelerating field decreases during propagation, the kinetic energy difference saturates, and dispersion translates the built-up energy correlation into a temporal correlation (panels iii & iv).

In the transmission electron microscope (JEM F200, JEOL) (see Fig. 1a), we generate few-particle electron pulses by close-to-threshold photoemission from a Schottky emitter [8, 32, 33, 40] with a femtosecond laser (2 MHz repetition rate, 160 fs pulse duration and 515 nm wavelength). The number of electrons emitted by each laser pulse follows moderately antibunched statistics [8], with a power-dependent rate of multi-electron emission events. The electron pulses are accelerated to 7 keV in an emitter assembly consisting of an extraction and focusing electrode and subsequently to a beam energy of $E_0 = 200$ keV (corresponding to a speed $v \approx 0.7c$). For spectral analysis, we use an energy filter and an event-based camera with nanosecond time resolution based on the Timepix3 ASIC [55] that allows us to classify the electron pulses according to their electron number.

The ensemble phase-space densities are reconstructed by ultrafast gating of the electron pulses. Conceptually, we relate $\rho_N(\{t_i\}, \{E_i\})$ to measurable electron energy spectra by exploiting inelastic electron-light scat-

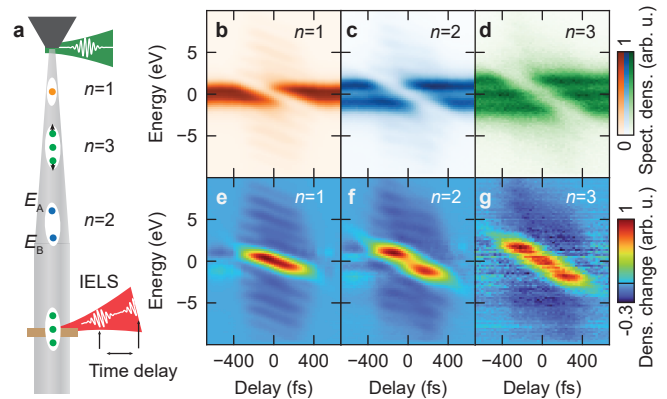


Figure 2. Inelastic electron-light scattering of few-electron pulses. a) Coulomb-correlated electron pulses traverse a time-delayed optical near field at a silicon membrane and undergo inelastic electron-light scattering. b-d) Pump-probe delay scans of pulse charge-resolved components $n = 1$ (panel b), $n = 2$ (panel c) and $n = 3$ (panel d) for inelastic few-electron-light scattering. e-g) Plot of spectral density change obtained by subtracting the spectrum at large time delays. As the optical near field scatters the temporally overlapped electrons, this spectrogram unveils the temporal separation of electrons within a pulse.

tering (IELS), a process where electrons are efficiently coupled to optical near fields [32, 33, 50, 54]. Here, few-electron states arriving in coincidence with an out-of-plane-polarized optical near field in the sample plane at time t_L are inelastically scattered by multiples of the photon energy. In this regard, as shown in the Appendix B, the recorded spectral maps $\langle \Gamma(t_L, \{E_i\}) \rangle$ can be written as the multi-dimensional convolution (\cdot symbol)

$$\langle \Gamma(t_L, \{E_i\}) \rangle = \frac{1}{N} \rho_N(t_L, \{E_i\}) \cdot P(t_L, \{E_i\}), \quad (1)$$

between the N -body phase-space density $\rho_N(\{t_{0,i}\}, \{E_{0,i}\})$ and the IELS slicing function $P(\{t_{0,i}\}, \{E_{0,i}\}) = \prod_{i=1}^N \Gamma(t_L - t_{0,i}, E_i - E_{0,i})$ over the delay times $\{t_{0,i}\}$ and energies $\{E_{0,i}\}$ of the electrons entering the IELS scattering region.

We begin characterising the few-electron states by acquiring pump-probe spectrograms as sketched in Fig. 2a. In these experiments, we focus the electron beam onto a silicon membrane. An optical near-field is created under illumination by femtosecond laser pulses of a center photon energy $\hbar\omega_L = 1.72$ eV and a full-width-at-half-maximum intensity duration of $\approx 1.67\Delta_L \approx 120$ fs. The electrons traversing the optical near-field at the membrane experience IELS with an electron-light coupling strength $|\beta| \sim 5.7$. Figure 2b-d shows optical-pump-electron-probe delay scans, sorted with respect to the number of electrons in the pulse. At large delays, we identify the characteristic single-, double- and triple-lobed spectra of $n = 1 - 3$ electron states [8]. As the temporal overlap is approached, electrons are inelastically

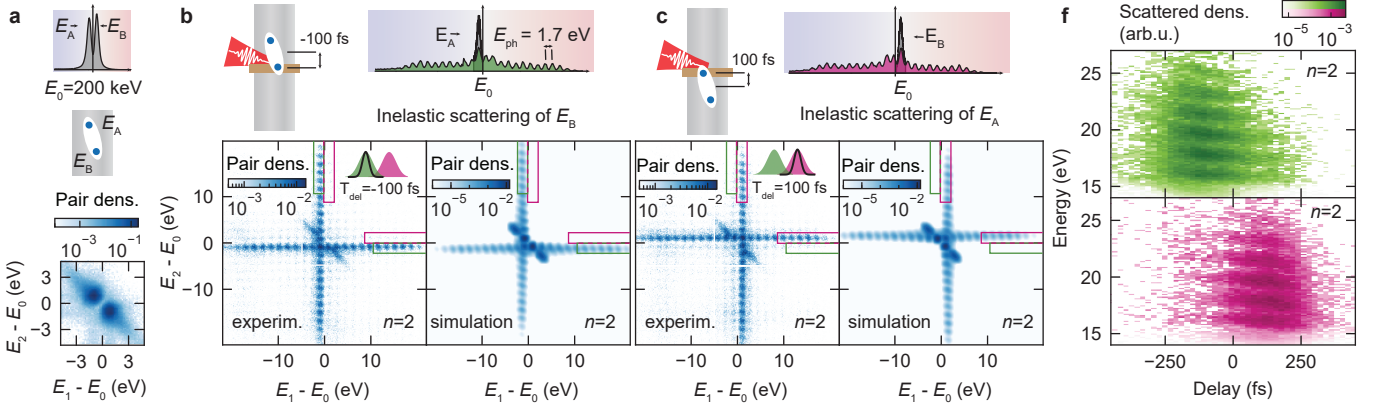


Figure 3. Phase-space reconstruction of double-electron states via inelastic electron-light scattering. a) Spectrum (top), scheme (middle) and electron energy pair histogram (bottom) of the bare Coulomb correlated $n = 2$ -state. b,c) Top: Upon interaction with a time-delayed short pump pulse, the faster electron (b) or the slower electron (c) of the $n = 2$ -state are selectively scattered at the optical near field, while the slower or faster electron is not scattered. Bottom: Inelastic electron-light scattering pair histograms of energies $E_{1/2}$ for coincident electrons A (the slower electron) and B (the faster electron) at pump-probe time delays of -100 fs (b) and 100 fs (c) and simulated correlation histogram at both time delays. The green and pink rectangles represent the first and second electron's energy gain regions, respectively. f) Gain-filtered IELS spectra of faster (green) and slower (pink) electron of two-electron states.

scattered to higher and lower energies, and the zero-loss peak is depleted. This is evident in the plot of the IELS-induced change in spectral density in Fig. 2e-g, defined as the delay-dependent spectrum subtracted by the spectrum at large delays $\langle \Gamma(t_L, \{E_i\}) \rangle - \langle \Gamma(t_L^{\max}, \{E_i\}) \rangle$. We identify a single-, double- and triple-peaked region for number states $n = 1 - 3$, showing that the electrons within a state have different arrival times at the sample plane.

For a quantitative analysis, we consider the electrons that were scattered to high sideband orders near the peak intensity of the laser pulse. Generally, this approach can be adopted to any number of electrons with a well-defined energy separation. In particular, we investigate electron pulses containing two electrons. These states exhibit a spectral double-lobe feature with an energy gap of 1.8 eV between the electrons, visible in the pair correlation histogram (see Fig. 3a). The general use of only a single laser pulse in IELS experiments, providing one single reference time t_L , prevents the full reconstruction of the multi-particle correlations through $\rho_N(\{t_i\}, \{E_i\})$ [see Eq. (1)]. However, its marginal $\rho_N(t, E)$ is accessible, as described in the following.

The analysis is simplified by the observation that experimentally, throughout the delay range, at most one of the two electrons undergoes IELS. This follows from a sufficient temporal separation of the energetically separated electrons. We assign the initially slower electron, which arrives later at the sample, the energy E_A , while the initially higher energy is denoted E_B . We generate an optical near field at pump-probe delay t_L to selectively scatter the faster (Fig. 3b, upper panel) or the slower (Fig. 3c, upper panel) of the correlated electrons for negative and positive pump-probe delays of $t_L = -100$ fs and $t_L = 100$ fs, respectively. Two-dimensional pair density

maps in terms of the two measured energies E_1 and E_2 after the interaction illustrate the selective interaction with the initially faster or slower electron, shown in the lower panels of Fig. 3b&c. In both cases, electrons are scattered from their initially separated energies (Fig. 3a) along the E_1 and E_2 axes. Importantly, the generated IELS combs have offsets that depend on the pump-probe delay. Specifically, the green or pink open-ended rectangles are selective electron-gain filters for the faster or slower electron, respectively. In our analysis, we identify the gain-scattered electron contributions from these regions, and the extracted electron energy- and delay-dependent densities are shown in Fig. 3f. The gain contributions are separated in time, but overlap to some extent at small delays. Under the assumption of short laser-pulse durations compared with the temporal profile of the electron pulses, this procedure allows us to connect the different contributions forming the 2-dimensional phase-space density $\rho_2(t, E) = \rho_A(t, E) + \rho_B(t, E)$, to the relative intensities, I_A for the pink and I_B for the green selected regions, of the filtered spectrograms, which are now given by the convolutions

$$I_{A,B}(t_L, E_2) \approx \frac{1}{2} \rho_{A,B}(t_L, E_2) \cdot \Gamma(t_L, E_2), \quad (2)$$

(see Appendix C and Refs. [32, 33, 50, 56]). Therefore, the data analysis required to obtain ρ simplifies to a deconvolution of Eqs. (2), carried out by a standard procedure. We Fourier transform the gain-filtered electron density at each time delay along the spectral axis. Then, we extract the phase of the Fourier transformation at the Fourier frequency of the photon energy to obtain the spectral phase of the IELS modulation, which corresponds to the momentary chirp $E_{A,B}^{\text{chirp}}(t)$. Together with the extracted spectral width from the Gaussian en-

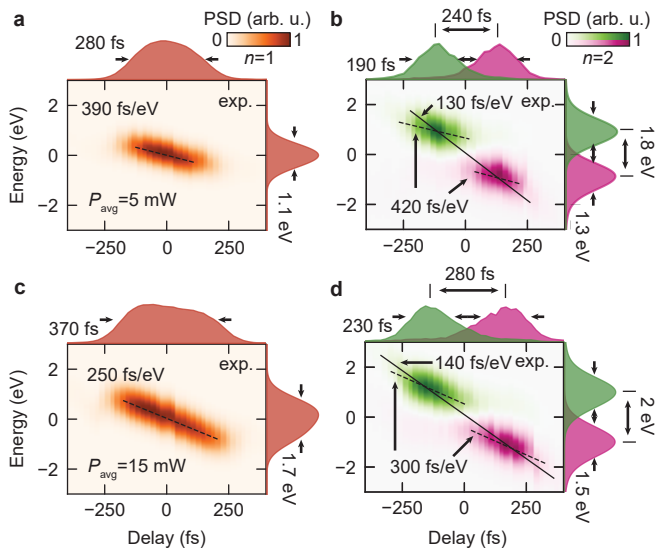


Figure 4. Reconstructed marginalized phase space densities of single- (a&c) and double-electron states (b&d) at the sample plane for photoemission laser powers of 5 mW (a&b) and 15 mW (c&d) incident onto the field emitter. The dashed lines are linear fits, revealing a single-electron pulse chirp of 390 fs/eV and 250 fs/eV for the two laser powers, respectively. The linear fits in b&d yield reduced chirps of 420 fs/eV (b) and 300 fs/eV (d) of the sub-ensembles. In comparison, the slope between the two maxima of the phase-space distributions (solid lines) are 130 fs/eV (b) and 140 fs/eV (d), respectively.

velope of the Fourier transform, we retrieve the slice of the two-electron phase space distribution $\rho_2(t, E)$ at the electrons' arrival time in the sample plane (see Appendix C).

The resulting phase space densities of the single and double-electron pulses shown in Fig. 4 are clearly distinct. While the single-electron distribution exhibits one lobe, the two-electron pulse distribution is bimodal with two regions spectrally and temporally separated by 1.8 eV and 240 fs, respectively (Fig. 4a&b). In general, the phase-space densities are affected by mean-field and stochastic interaction close to the emitter [32, 33], resulting in an electron pulse chirp that depends on the photoemission current and that is also affected by scattering with electrons not entering the beam (compare the upper and lower panels in Fig. 4). We see a similar chirp and current-dependent change thereof for the phase-space distribution of single-electron pulses and for the sub-ensembles constituting the two-electron pulse. Specifically, this chirp decreases from a value around 400 fs/eV at lower current to a value near or below 300 fs/eV at higher current. In contrast, the two separate lobes of the two-electron distribution are displaced by an effective chirp of 130-140 fs/eV that only weakly depends on photocurrent (solid lines in Fig. 4b,d). First, the apparent independence of this inter-electron chirp on laser power illustrates that the strength of the Coulomb correlation is

hardly influenced by auxiliary electrons not entering the beam [8]. Second, the lower chirp value between the two parts of the bimodal distribution compared to the chirp within the sub-ensembles reflects the fact that the energy difference of the electrons emerges during propagation. This in turn causes reduced dispersion as compared to that experienced by variation in initial conditions upon photoemission. We note that these features of the experimentally retrieved longitudinal phase-space distributions of double-electron states are also reproduced by the trajectory simulations discussed in Fig. 1b. Considering further details of the distributions, we recognize a non-linear distortion in the experimentally reconstructed two-electron densities, flattening out towards zero delay and increasing towards larger absolute delays. This higher-order chirp (cf. Fig. 4b, and also Fig. 3f) suggests a correlation of the final electron energy difference with the remaining dispersion during propagation. Specifically, stronger scatterings tend to occur closer to the emitter, leaving a larger influence of dispersion after the interaction, while weaker interactions coincide with lower total dispersion.

In summary, we numerically and experimentally mapped a Coulomb-induced splitting of the two-electron phase-space distribution in an ultrafast transmission electron microscope beam. To reconstruct multi-electron phase-space distributions, we expanded the theoretical framework of the quantum inelastic electron-light interaction to multiple electrons, including the effect of classical averaging over electron ensembles. In particular, we connected the spectrograms and the N -particle phase-space density that fully characterizes all beam properties through a simple multi-dimensional convolution (see Eq. (1)). While the full $\rho_N(\{t_i\}, \{E_i\})$ cannot be accessed via single-pulse IELS, its marginals are retrieved by inverting a one-dimensional convolution obtained by filtering the gain part of the spectrum relative to the interaction with each electron (Eq. (2)). Electrons emitted by the same laser pulse mutually exchange energy over an acceleration distance of centimetres, thereby acquiring a velocity difference that leads to arrival time separations on the order of ≈ 200 fs at the sample plane. Generally, the framework of inelastic few-electron-light scattering opens various avenues to modulate and control electron number states with, e.g., light pulses tailored to the densities of the individual electrons. Future studies involving N femtosecond-separated laser pulses with adjustable delays may address the reconstruction of the full longitudinal phase-space distribution of an N -electron beam phase-space distribution $\rho_N(\{t_i\}, \{E_i\})$ and utilize the density modulation to induce superradiance in bosonic or fermionic quantum systems.

ACKNOWLEDGEMENTS

We acknowledge the continued support from the Göttingen UTEM team. We thank Thomas Rittmann for

insightful discussions on phase space density reconstruction. The experiments were conducted at the Göttingen UTEM Lab, funded by the Deutsche Forschungsgemeinschaft (German Research Foundation) through Project-ID 432680300 (SFB 1456, project C01 to C.R.), the Gottfried Wilhelm Leibniz program (RO 3936/4-1 to C.R.) and the European Union's Horizon 2020 research and innovation programme under grant agreement no. 101017720 (FET-Proactive EBEAM).

AUTHOR CONTRIBUTIONS

C.R. directed the study. R.H. conducted the experiments and data analysis with contributions from A.F. R.H. prepared the figures, with contributions from V.D.G. R.H. and V.D.G. conducted particle simulations. V.D.G. developed the theoretical framework. All authors discussed the results and interpretation. R.H., V.D.G., and C.R. wrote the manuscript with input and feedback from A.F.

COMPETING INTERESTS

The authors declare no competing interests.

APPENDIX

Appendix A: Trajectory simulations

The few-electron phase-space distributions were simulated with a relativistic particle trajectory simulation. In our model, we numerically integrate the equations of motion of particles mutually interacting via Coulomb's force and propagating in a static electric field

$$\frac{d\mathbf{p}_i(t)}{dt} = \frac{e^2}{4\pi\epsilon_0} \sum_{j \neq i}^N \frac{\mathbf{r}_i - \mathbf{r}_j}{|\mathbf{r}_i - \mathbf{r}_j|^3} + e\mathbf{E}_{\text{static}}(\mathbf{r}_i), \quad (\text{A1})$$

where \mathbf{p}_i , \mathbf{r}_i , e and m_e are the relativistic momentum, position, charge, and rest mass of the i^{th} electron. Its velocity is calculated using the relation

$$\mathbf{p}_i = \gamma m_e \mathbf{v}_i = \frac{m\mathbf{v}_i}{\sqrt{1 - |\mathbf{v}_i|^2/c^2}}. \quad (\text{A2})$$

The electrons are accelerated in a static two-stage electric field $E_{\text{static}}(\mathbf{r}_i) = E_{\text{ext}}(\mathbf{r}_i) + E_{\text{acc}}(\mathbf{r}_i)$. Here, the first summand corresponds to the non-linear extraction field

$$E_{\text{ext}}(\mathbf{r}) = \frac{U_{\text{ext}}}{r_{\text{tip}}^{-1} - R_{\text{ext}}^{-1}} \frac{\mathbf{r}}{r^3}, \quad (\text{A3})$$

with extraction voltage $U_{\text{ext}} = 2$ kV, tip radius $r_{\text{tip}} = 1$ μm , and the distance of the extractor from the tip

$R_{\text{ext}} = 500$ μm . The second summand is a constant axial accelerating electric field

$$E_{\text{acc}}(\mathbf{r}) = \begin{cases} U_{\text{acc}}/d_{\text{acc}} \cdot \mathbf{e}_z & \text{if } r_z \leq d_{\text{acc}}, \\ 0 & \text{if } r_z > d_{\text{acc}}, \end{cases} \quad (\text{A4})$$

where $U_{\text{acc}} = 198$ kV is the accelerating voltage of the transmission electron microscope and $d_{\text{acc}} = 0.85$ m is the distance over which the electrons are accelerated. Finally, we account for jitter in the high tension and limited experimental energy resolution by an incoherent temporal averaging of $t_{\text{res}} = 70$ fs and spectral averaging of $E_{\text{res}} = 0.3$ eV.

For each simulation run, the electrons are randomly distributed in position within an area of radius 170 nm on a 1 μm -sized spherical tip. The emission time and excess energy of the electrons is normally distributed with root-mean-square widths of 80 fs and 0.35 eV, respectively. The ratio between the initial longitudinal v_{long} and transverse v_{trans} velocity components $v_{\text{trans}}/v_{\text{long}}$ is given by $\tan(\theta)$ and θ is uniformly distributed in the interval -2° and 2° .

Appendix B: Multi-electron IELS theory for short laser pulses

The theoretical description of the energy correlation maps showed in the main text can be carried out through a N -electron generalization of the well-established formulation of IELS experiments performed in electron microscopes with acceleration voltages in the kV range [57–59]. In this regime, the minimal coupling Hamiltonian, describing the interaction of N swift electrons travelling with velocities $\{\mathbf{v}_i\}$ with a classical time-varying vector potential $\mathbf{A}(\mathbf{r}, t)$, can be simplified by linearizing the electrons' dispersion relation around a single central momentum \mathbf{k}_0 , taken to be the average momentum, corresponding to the relativistic energy $E_0 = c\sqrt{m_e^2 c^2 + \hbar^2 k_0^2}$ and to the velocity $\mathbf{v} = (\hbar c^2/E_0)\mathbf{k}_0$. By further neglecting spin flips, ponderomotive forces, small differences of the order $|\mathbf{v} - \mathbf{v}_i|/c \sim 10^{-5}$ between electrons' velocities, and Coulomb repulsion close to the Si membrane, we can solve the Schrödinger equation $i\hbar\partial_t\psi^i(\mathbf{r}_i, t) = \mathcal{H}^i\psi^i(\mathbf{r}_i, t)$ for each i -electron separately with Hamiltonian $\mathcal{H}^i = E_0 - \hbar\mathbf{v} \cdot (i\nabla_{\mathbf{r}_i} + \mathbf{k}_0) + (e\mathbf{v}/c) \cdot \mathbf{A}(\mathbf{r}_i, t)$, which admits the analytical solution

$$\psi^i(\mathbf{r}_i, t) = \psi_0^i(\mathbf{r}_i, t) \times \exp \left\{ (-ie/\hbar c) \int_{-\infty}^t dt' \mathbf{v} \cdot \mathbf{A}[\mathbf{r}_i - \mathbf{v}(t-t'), t'] \right\} \quad (\text{B1})$$

for an initial wave function $\psi_0(\mathbf{r}_i, t) = e^{i(\mathbf{k}_0 \cdot \mathbf{r}_i - E_0 t/\hbar)} \phi_0^i(\mathbf{r}_i - \mathbf{v}t)$ entering the interaction zone. We now focus our attention on a semi-monochromatic laser pulse at frequency ω_L for which the vector potential can be described by a slowly varying electric-field envelope with a negligible time derivative $\vec{\mathcal{E}}(\mathbf{r}, t)$ as

$\mathbf{A}(\mathbf{r}, t) = (-ic/\omega_L)\vec{\mathcal{E}}(\mathbf{r}, t)e^{-i\omega_L t} + \text{c.c.}$. Eq. (B1) can be reformulated in terms of a superposition of amplitudes describing the loss and gain of ℓ light quanta ($\ell > 0$ for gain and $\ell < 0$ for loss) by each individual electron via the Jacobi-Anger expansion $e^{iu \sin \theta} = \sum_{\ell} J_{\ell}(u)e^{i\ell\theta}$ [Eq. (9.1.41) of Ref. 60]. By doing so, Eq. (B1) transforms into

$$\psi^i(\mathbf{r}_i, t) = \psi_0^i(\mathbf{r}_i, t) \sum_{\ell=-\infty}^{\infty} J_{\ell}(2|\beta(\mathbf{r}, t)|) e^{i\ell\varphi(\mathbf{r}_i, t)}, \quad (\text{B2})$$

with $\varphi(\mathbf{r}_i, t) = \arg\{-\beta(\mathbf{r}_i, t)\}$ written in terms of the time-dependent coupling coefficient $\beta(\mathbf{r}, t) = (e/\hbar\omega_L) \int_{-\infty}^t dt' \mathbf{v} \cdot \vec{\mathcal{E}}[\mathbf{r} - \mathbf{v}(t - t'), t] e^{-i\omega_L t'}$. We now take the electrons to propagate along the z -axis while modeling the laser pulse, arriving at time t_L at the sample, with the temporal Gaussian profile $\vec{\mathcal{E}}(\mathbf{r}, t) = \vec{\mathcal{E}}(\mathbf{r})e^{-(t-t_L)^2/2\Delta_L^2}$. For the duration of the laser pulses (tens of fs), electron coherence times (few fs), and interaction times (sub-fs), used in this work, we can approximate $\beta(\mathbf{r}, t) \approx e^{-[z/v - (t-t_L)]^2/2\Delta_L^2 - i\omega_L(t-z/v)}\beta$ with $\beta = (e/\hbar\omega_L) \int_{-\infty}^z dz' \mathcal{E}_z(\mathbf{R}, z') e^{-i\omega_L z'/v}$. By plugging $\beta(\mathbf{r}, t)$ into Eq. (B2), we obtain

$$\psi^i(\mathbf{r}_i, t) = \psi_0^i(\mathbf{r}_i, t) \mathcal{P}(\mathbf{R}_i, z_i - vt)$$

where the IELS amplitude $\mathcal{P}(\mathbf{R}, z) = \sum_{\ell=-\infty}^{\infty} J_{\ell}[2e^{-(z/v-t_L)^2/2\Delta_L^2} |\beta|] e^{i\ell(\omega_L z/v + \varphi)}$ and $\varphi = \arg\{-\beta\}$. The probability $P(\{E_i\}) = \prod_i \Gamma_i(E_i)$ of measuring the N electrons in a set of energies $\{E_i\}$ is directly connected to their wave functions via the one-dimensional spatial Fourier transform $\Gamma_i(E_i) = (1/2\pi\hbar v) \int d\mathbf{R} \left| \int_{-\infty}^{\infty} dz \psi_0^i(\mathbf{r}) e^{-i[k_0 + (E_i - E_0)/\hbar]z} \right|^2$.

For a Gaussian electron of main energy $E_{0,i}$ and coherence time Δ_c , focused around the transversal coordinate \mathbf{R}_0 , and crossing the $z_{0,i} = t_{0,i}/v$ plane at $t = 0$, we can write $\psi_0^i(\mathbf{r}) = \sqrt{\delta(\mathbf{R} - \mathbf{R}_0)} e^{ik_{0,i}z - (z-z_{0,i})^2/4v^2\Delta_c^2} / (2\pi v^2 \Delta_c^2)^{1/4}$. For such state, the Fourier transform can be carried out exactly by using the expansion $J_{\ell}(x) = \text{sign}^{\ell} \sum_{m=0}^{\infty} (-1)^m (x/2)^{2m+|\ell|} / m!(m+|\ell|)!$. The resulting expression can be further simplified by neglecting terms of order $(\Delta_c/\Delta_L)^4$ and considering $\omega_L \Delta_c \gg 1$, and is given by $\Gamma_i(E_i) = \Gamma(t_L - t_{0,i}, E_i - E_{0,i})$ with

$$\Gamma(t, E) = \frac{\Delta_c}{\hbar} \sum_{\substack{\ell=-\infty \\ m, m'=0}}^{\infty} b_{mm'\ell} e^{-nt^2/\lambda\Delta_L^2 - 2[E/\hbar - \ell\omega_L]^2\Delta_c^2}, \quad (\text{B3})$$

where $\lambda = 1 + 4n\Delta_c^2/\Delta_L^2$, $n = |\ell| + m + m'$, and $b_{mm'\ell} = (-1)^{m+m'} |\beta|^{2n} \sqrt{2}/\sqrt{\pi\lambda} m!m'!(|\ell|+m)!(|\ell|+m')!$.

Finally, the recorded energy maps $\langle \Gamma(t_L, \{E_i\}) \rangle$ will be the result of the incoherent average of the N -electron IELS spectra $P(\{E_i\}) = \prod_{i=1}^N \Gamma(t_L - t_{0,i}, E_i - E_{0,i})$, acting as convolution function, over the classical $\rho_N(\{t_{0,i}\}, \{E_{0,i}\})$ ensemble of delays $\{t_{0,i}\}$ and energies

$\{E_{0,i}\}$ at the membrane plane, namely, Eq. (1). The factor $1/N$ originates from the normalization condition $N = \int \{dE_i\} \{dt_i\} \rho_N(\{t_i\}, \{E_i\})$. In particular, the simulated maps in Fig. (3b,c) have been computed by using the two-electron phase-space density obtained from the trajectory simulations [see Fig. (1)] while setting $\Delta_L = 72$ fs, $\Delta_c = 1.83$ fs, and $\beta = 5.68$.

Appendix C: Slicing and reconstruction algorithm

Because indistinguishable, the two-electron phase-space density $\rho_2(t_1, t_2, E_1, E_2)$ will be symmetric under exchange of electron labels and therefore its marginalized distribution can be expressed as the sum of two contributions $\rho_2(t, E) = \rho_A(t, E) + \rho_B(t, E)$. In particular, because of Coulomb repulsion, these components will be localized in energy and time around the values $(\bar{E}_A, \bar{t}_A) < (\bar{E}_B, \bar{t}_B)$ [see Fig. (1)]. The slicing procedure leverages such time and energy localization to extract them from different parts of the spectrograms. Indeed, under the assumption that Δ_L is small compared to the temporal separation between ρ_A and ρ_B , one can integrate over E_1 the maps $\langle \Gamma(t_L, E_1, E_2) \rangle$ for each value of E_2 in the green (for $t_L \sim \bar{t}_B$) and pink (for $t_L \sim \bar{t}_A$) top selection regions of Fig. (3b,c) (or equivalently swapping the roles of E_1 and E_2 for the rightmost selection regions), to reduce Eq. (1) into the two one-dimensional convolutions reported in Eq. (2).

In order to obtain the marginalized phase-space densities, we make two other approximations: (i) short laser-pulse duration compared to the temporal extension of the distributions ($\Delta_L/\sqrt{n} \sim 30$ fs for the outermost energy sidebands); (ii) the energy and time dependencies can be expressed in the form $\rho_{A,B}(t, E) = n_{A,B}(t) e^{-[E - E_{A,B}^{\text{chirp}}(t) - \bar{E}_{A,B}]^2/2\sigma_{\text{inc}}^2} / \sqrt{2\pi\sigma_{\text{inc}}^2}$, i.e., an incoherent Gaussian energy envelope of standard deviation σ_{inc} with chirp function $E_{A,B}^{\text{chirp}}(t)$ multiplied by an unknown time-dependent distribution $n_{A,B}(t)$ is assumed. After plugging this form into Eq. (2) and by using Eq. (B3) in the energy regions of interest, we obtain

$$I_{A,B}(t_L, E_2) \approx C n_{A,B}(t_L) \sum_{\ell=\ell_{\min}}^{\ell_{\max}} a_{\ell} e^{-[E_B - E_{A,B}^{\text{chirp}}(t_L) - \bar{E}_{A,B} - \ell\hbar\omega_L]^2/2\sigma^2}, \quad (\text{C1})$$

where $\sigma^2 = \hbar^2/4\Delta_c^2 + \sigma_{\text{inc}}^2$, C and a_{ℓ} are real-valued coefficients, and the summation over ℓ has been limited to the range $[\ell_{\min}, \ell_{\max}]$ to account for the finite number of selected sidebands. Finally, $E_{A,B}^{\text{chirp}}(t)$ is extracted from the phase of the Fourier transform of Eq. (C1), performed along the energy axis and subtracting a constant phase such that $E_{A,B}^{\text{chirp}}(\bar{t}_{A,B}) = 0$, while, the temporal profile $n_{A,B}(t)$ follows after the integration of Eq. (C1) over E_2 and by normalizing the result.

- * valerio.digiulio@mpinat.mpg.de
† claus.ropers@mpinat.mpg.de
- [1] H. Boersch, *Zeitschrift für Physik* **139**, 115 (1954).
 - [2] KH. Loeffler, *Zeitschrift für angewandte Physik* **27**, 145 (1969).
 - [3] S. Borrelli, T. C. H. de Raadt, S. B. van der Geer, P. H. A. Mutsaers, K. A. H. van Leeuwen, and O. J. Luiten, *Physical Review Letters* **132**, 115001 (2024).
 - [4] H. Kiesel, A. Renz, and F. Hasselbach, *Nature* **418**, 392 (2002).
 - [5] T. Kodama, N. Osakabe, and A. Tonomura, *Physical Review A* **83**, 063616 (2011).
 - [6] M. Kuwahara, Y. Yoshida, W. Nagata, K. Nakakura, M. Furui, T. Ishida, K. Saitoh, T. Ujihara, and N. Tanaka, *Physical Review Letters* **126**, 125501 (2021).
 - [7] S. Keramati, W. Brunner, T. J. Gay, and H. Batelaan, *Physical Review Letters* **127**, 180602 (2021).
 - [8] R. Haindl, A. Feist, T. Domröse, M. Möller, J. H. Gaida, S. V. Yalunin, and C. Ropers, *Nature Physics* **19**, 1410 (2023).
 - [9] P. Hommelhoff, Y. Sortais, A. Aghajani-Talesh, and M. A. Kasevich, *Physical Review Letters* **96**, 077401 (2006).
 - [10] C. Ropers, D. R. Solli, C. P. Schulz, C. Lienau, and T. Elsaesser, *Physical Review Letters* **98**, 043907 (2007).
 - [11] B. Barwick, C. Corder, J. Strohaber, N. Chandler-Smith, C. Uiterwaal, and H. Batelaan, *New Journal of Physics* **9**, 142 (2007).
 - [12] S. Meier, J. Heimerl, and P. Hommelhoff, *Nature Physics* **19**, 1402 (2023).
 - [13] S. A. Koppell, J. W. Simonaitis, M. A. R. Krielaart, W. P. Putnam, K. K. Berggren, and P. D. Keathley, Analysis and Applications of a Heralded Electron Source (2024), [arXiv:2406.18755](https://arxiv.org/abs/2406.18755) [physics].
 - [14] A. Gover and A. Yariv, *Physical Review Letters* **124**, 064801 (2020).
 - [15] Z. Zhao, X.-Q. Sun, and S. Fan, *Physical Review Letters* **126**, 233402 (2021).
 - [16] A. Karnieli, N. Rivera, A. Arie, and I. Kaminer, *Physical Review Letters* **127**, 060403 (2021).
 - [17] F. J. García de Abajo and V. Di Giulio, *ACS Photonics* **8**, 945 (2021).
 - [18] D. Rätzl, D. Hartley, O. Schwartz, and P. Haslinger, *Physical Review Research* **3**, 023247 (2021).
 - [19] B. Zhang, D. Ran, R. Ianculescu, A. Friedman, J. Scheuer, A. Yariv, and A. Gover, *Physical Review Letters* **126**, 244801 (2021).
 - [20] R. Ruimy, A. Gorlach, C. Mechel, N. Rivera, and I. Kaminer, *Physical Review Letters* **126**, 233403 (2021).
 - [21] O. Kfir, V. Di Giulio, F. J. G. de Abajo, and C. Ropers, *Science Advances* **7**, eabf6380 (2021).
 - [22] V. Di Giulio, O. Kfir, C. Ropers, and F. J. García de Abajo, *ACS Nano* **15**, 7290 (2021).
 - [23] A. Gorlach, O. Reinhardt, A. Pizzi, R. Ruimy, G. Baranes, N. Rivera, and I. Kaminer, *Physical Review A* **109**, 023722 (2024).
 - [24] E. J. VandenBussche and D. J. Flannigan, *Nano Letters* **19**, 6687 (2019).
 - [25] J. J. Axelrod, J. T. Zhang, P. N. Petrov, R. M. Glaeser, and H. Müller, *Current Opinion in Structural Biology* **86**, 102805 (2024).
 - [26] O. Kfir, *Physical Review Letters* **123**, 103602 (2019).
 - [27] N. Talebi and I. Březinová, *New Journal of Physics* **23**, 063066 (2021).
 - [28] A. Konečná, F. Iyikanat, and F. J. García de Abajo, *Science Advances* **8**, eabo7853 (2022).
 - [29] E. Kazakevich, H. Aharon, and O. Kfir, *Physical Review Research* **6**, 043033 (2024).
 - [30] J.-W. Henke, H. Jeng, and C. Ropers, *Quantum eraser experiments for the demonstration of entanglement between swift electrons and light* (2024), [arXiv:2404.11368](https://arxiv.org/abs/2404.11368).
 - [31] A. H. Zewail, *Science* **328**, 187 (2010).
 - [32] A. Feist, N. Bach, N. Rubiano da Silva, T. Danz, M. Möller, K. E. Priebe, T. Domröse, J. G. Gatzmann, S. Rost, J. Schauss, S. Strauch, R. Bormann, M. Sivis, S. Schäfer, and C. Ropers, *Ultramicroscopy* **176**, 63 (2017).
 - [33] N. Bach, T. Domröse, A. Feist, T. Rittmann, S. Strauch, C. Ropers, and S. Schäfer, *Structural Dynamics* **6**, 014301 (2019).
 - [34] P. K. Olshin, M. Drabbels, and U. J. Lorenz, *Structural Dynamics* **7**, 054304 (2020).
 - [35] C. Zhu, D. Zheng, H. Wang, M. Zhang, Z. Li, S. Sun, P. Xu, H. Tian, Z. Li, H. Yang, and J. Li, *Ultramicroscopy* **209**, 112887 (2020).
 - [36] R. Shiloh, T. Chlouba, and P. Hommelhoff, *Physical Review Letters* **128**, 235301 (2022).
 - [37] J. Kuttruff, D. Nabben, A.-C. Zimmermann, A. Ryabov, and P. Baum, *Science Advances* **10**, eadl6543 (2024).
 - [38] A. Schröder, A. Wendeln, J. T. Weber, M. Mukai, Y. Kohno, and S. Schäfer, Laser-driven cold-field emission source for ultrafast transmission electron microscopy (2024), [arXiv:2410.23961](https://arxiv.org/abs/2410.23961) [physics].
 - [39] D. H. Dowell and J. F. Schmerge, *Physical Review Special Topics - Accelerators and Beams* **12**, 074201 (2009).
 - [40] B. Cook, M. Bronsgeest, K. Hagen, and P. Kruit, *Ultramicroscopy* **109**, 403 (2009).
 - [41] G. Herink, D. R. Solli, M. Gulde, and C. Ropers, *Nature* **483**, 190 (2012).
 - [42] M. Krüger, M. Schenk, and P. Hommelhoff, *Nature* **475**, 78 (2011).
 - [43] G. Hergert, R. Lampe, A. Wöste, and C. Lienau, *Nano Letters* **24**, 11067 (2024).
 - [44] B. Cook and P. Kruit, *Applied Physics Letters* **109**, 151901 (2016).
 - [45] M. Kuwahara, Y. Nambo, K. Aoki, K. Sameshima, X. Jin, T. Ujihara, H. Asano, K. Saitoh, Y. Takeda, and N. Tanaka, *Applied Physics Letters* **109**, 013108 (2016).
 - [46] S. Meier and P. Hommelhoff, *ACS Photonics* **9**, 3083 (2022).
 - [47] C. T. Hebeisen, G. Sciaini, M. Harb, R. Ernstorfer, T. Dartigalongue, S. G. Kruglik, and R. J. D. Miller, *Optics Express* **16**, 3334 (2008).
 - [48] M. Kozák, J. McNeur, K. J. Leedle, H. Deng, N. Schönenberger, A. Ruehl, I. Hartl, J. S. Harris, R. L. Byer, and P. Hommelhoff, *Nature Communications* **8**, 14342 (2017).
 - [49] D. Epp, B. Schröder, M. Möller, and C. Ropers, *Structural Dynamics* **11**, 024306 (2024).
 - [50] S. T. Park, O.-H. Kwon, and A. H. Zewail, *New Journal of Physics* **14**, 053046 (2012).
 - [51] F. O. Kirchner, A. Gliserin, F. Krausz, and P. Baum, *Nature Photonics* **8**, 52 (2014).

- [52] B. Barwick, D. J. Flannigan, and A. H. Zewail, *Nature* **462**, 902 (2009).
- [53] F. J. García de Abajo, *Reviews of Modern Physics* **82**, 209 (2010).
- [54] A. Feist, K. E. Echternkamp, J. Schauss, S. V. Yalunin, S. Schäfer, and C. Ropers, *Nature* **521**, 200 (2015).
- [55] R. Ballabriga, M. Campbell, and X. Llopart, *Nuclear Instruments and Methods in Physics Research Section A: Accelerators, Spectrometers, Detectors and Associated Equipment* **878**, 10 (2018).
- [56] D. A. Plemmons, S. Tae Park, A. H. Zewail, and D. J. Flannigan, *Ultramicroscopy* **146**, 97 (2014).
- [57] S. T. Park, M. Lin, and A. H. Zewail, *New J. Phys.* **12**, 123028 (2010).
- [58] F. J. García de Abajo, A. Asenjo-Garcia, and M. Kociak, *Nano Lett.* **10**, 1859 (2010).
- [59] G. M. Vanacore, I. Madan, G. Berruto, K. Wang, E. Pomarico, R. J. Lamb, D. McGrouther, I. Kaminer, B. Barwick, F. J. García de Abajo, and F. Carbone, *Nat. Commun.* **9**, 2694 (2018).
- [60] M. Abramowitz and I. A. Stegun, *Handbook of Mathematical Functions* (Dover, New York, 1972).